Bragg Coherent Diffractive Imaging for Defects Analysis: Principles, Applications, and Challenges

Yifei Sun[1], Andrej Singer[1,]*
[1]*Department of Materials Science and Engineering, Cornell University, Ithaca, New York 14850, USA*
[*]asinger@cornell.edu

Abstract

The ability to visualize crystalline defects and lattice distortions at the nanoscale holds profound implications for enhancing material properties and optimizing their design. Bragg coherent diffractive imaging (BCDI) emerges as a powerful technique due to its simplicity and high sensitivity to lattice strains. This review critically examines recent advancements in BCDI, highlighting its capability to uncover defects under various experimental conditions. It discusses fundamental principles and data analysis intricacies, as well as BCDI's applications in characterizing structural and functional materials. Furthermore, it offers perspectives on the current limitations of BCDI and the potential implications of synchrotron upgrades. By providing these insights, the review enhances our understanding of BCDI's role in advancing materials science and nanotechnology.

I. Introduction

Crystalline defects and lattice distortions play a significant role in determining materials' mechanical, electrical, and chemical properties. With the continuing advancement in nanotechnology, the imperative to visualize these defects and distortions at the nanoscale is increasingly important for the design and optimization of functional materials. Several electron- and X-ray-based imaging techniques have emerged as powerful tools for resolving defects and strain in nanomaterials, including transmission electron microscopy[1], X-ray ptychographic topography[2], and scanning hard X-ray microscopy[3] .

The crux of defect imaging lies in achieving high spatial resolution and, for in-situ studies, necessitates high temporal resolution and adaptability to diverse experimental conditions. Under these conditions, Bragg coherent diffractive imaging (BCDI) is a powerful tool for imaging defects in crystalline nanoparticles given its relatively easy experimental setup and extreme sensitivity to lattice displacements and strain. Previous review papers on BCDI have discussed its efficacy in imaging strain at the nanoscale[4], probing systems across timescales ranging from nanoseconds to femtoseconds[5], and exploring its applications in electronic[6] and electrocatalytic[7] materials.

In this review, we focus on different types of defects that BCDI can unravel across various experimental conditions, particularly on recent advancements. Section II elucidates the fundamental principles of the experimental realization of BCDI, alongside the intricacies of data analysis and interpretation. Subsequently, Section III reviews BCDI applications in structural and functional materials, spanning ex-situ studies, multi-reflection techniques, in-situ investigations, and operando analyses. In the concluding section, we provide our perspectives on the current

limitations of BCDI and the implications of recent developments in synchrotron sources on addressing these challenges.

II. Principles

In recent decades, the development of X-ray sources has advanced rapidly. The newest-generation synchrotron sources offer a brilliance twelve orders of magnitude higher than conventional X-ray tubes with rotating anodes[8]. These improvements provide higher flux and larger spatial coherence, opening opportunities for advanced X-ray techniques on nanomaterials. Among these, BCDI combines the high spatial coherence and the extreme lattice sensitivity of the Bragg diffraction to image lattice distortions in nanocrystalline materials. Several synchrotrons have the capability to conduct BCDI experiments, including the Advanced Photon Source (APS), European Synchrotron Radiation Facility (ESRF), Diamond Light Source, PETRA III, MAX IV, Brazilian Synchrotron Light Laboratory, and Pohang Light Source (PLS-II).

In a BCDI experiment (Fig. 1), the incident coherent X-ray beam illuminates a nanocrystal. A 3D reciprocal space map around the crystal's reciprocal lattice point, $\boldsymbol{h}$, is acquired by rocking the crystal in an angle, ω, and collecting the diffraction images on an area detector. This procedure is equivalent to scanning the Ewald sphere over a region of the reciprocal space[9]. The samples include free-standing crystals, often synthesized directly on a substrate or by focused ion beam (FIB) patterning, or crystals in the powder form.

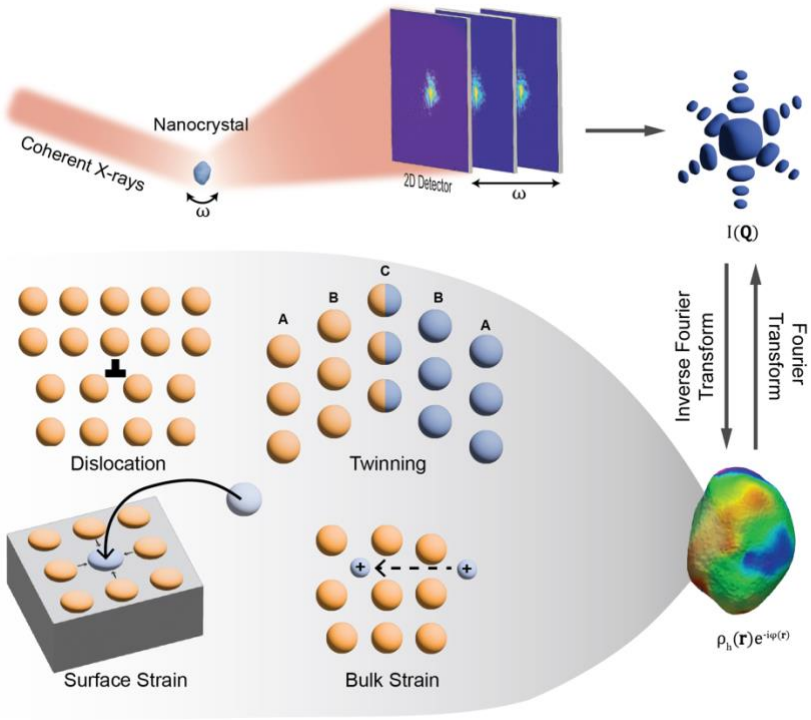

Figure 1. Schematic of the BCDI workflow. The incident coherent X-rays scatter off a nanocrystal and a 2D detector records the selected Bragg peak and its interference pattern. The crystal is rotated across an angle, ω, while the area detector measures the diffraction pattern at each step. These collective diffraction patterns form a 3D representation

of the Bragg peak with well-defined fringes. The diffraction intensity, $I(\boldsymbol{Q})$, is related to the complex density function, $\rho_{\boldsymbol{h}}(\boldsymbol{r})\mathrm{e}^{-i\varphi(\boldsymbol{r})}$, via Fourier transform (see eq. (1)). This complex density function encodes information about lattice displacements within the crystal, offering insights into crystalline defects like dislocations, twinning, surface strain, and bulk strain.

The resulting coherent diffraction pattern displays well-defined interference features, often referred to as fringes, which occur because of the crystal's finite size, analogous to single-slit scattering in optics[10]. Well-faceted crystals generate intensity flares perpendicular to the respective facets. The diffraction intensity $I(\boldsymbol{Q})$ is a function of momentum transfer $\boldsymbol{Q}$, where $\boldsymbol{Q} = \boldsymbol{q} - \boldsymbol{h}$ and $\boldsymbol{q} = \boldsymbol{k}_f - \boldsymbol{k}_i$. $\boldsymbol{k}_i$ and $\boldsymbol{k}_f$ are the incident and scattered wave vectors, respectively. The intensity is the squared modulus of the scattering amplitude, $A(\boldsymbol{Q})$, where $I(\boldsymbol{Q}) = |A(\boldsymbol{Q})|^2$. Under kinematic approximation, the scattering amplitude of a finite-sized crystal from coherent monochromatic radiation can be well estimated as[10],

$$A_{\boldsymbol{h}}(\boldsymbol{Q}) = F_{\boldsymbol{h}} \int s_{\boldsymbol{h}}(\boldsymbol{r})\mathrm{e}^{-i\boldsymbol{h}\cdot\boldsymbol{u}(\boldsymbol{r})}\mathrm{e}^{-i\boldsymbol{Q}\cdot\boldsymbol{r}}d\boldsymbol{r} \quad (1)$$

$F_{\boldsymbol{h}}$ is the unit cell structure factor, $\boldsymbol{r}$ is the coordinate in real space, $\boldsymbol{h}$ is the specific reciprocal lattice point measured during the experiment, and $\boldsymbol{u}(\boldsymbol{r})$ is the displacement from the ideal lattice point. Based on eq. (1), the scattering amplitude is related to the complex density function $S(\boldsymbol{r}) = s_{\boldsymbol{h}}(\boldsymbol{r})\mathrm{e}^{-i\boldsymbol{h}\cdot\boldsymbol{u}(\boldsymbol{r})}$ through a Fourier transform, where the amplitude, $s_{\boldsymbol{h}}(\boldsymbol{r})$, describes the presence of the scattering planes associated with the reciprocal lattice point $\boldsymbol{h}$. The displacement field, $\boldsymbol{u}(\boldsymbol{r})$, reports the local distortion from the reference lattice points of a perfect crystal. According to Friedel's law, the squared amplitude of a Fourier-transformed function is centrosymmetric when $S(\boldsymbol{r})$ is a real function[11]. Therefore, a perfect crystal that has $\boldsymbol{u}(\boldsymbol{r}) = 0$ results in a symmetric diffraction pattern with an identical shape around each reciprocal lattice point. The internal deformation from defects typically leads to a non-zero phase and introduces an asymmetry in the diffraction pattern[4,12,13].

A direct inversion of eq. (1) is impossible because only the squared modulus of $A(\boldsymbol{Q})$, $I(\boldsymbol{Q})$, is measured, and the phase of the complex field, $\mathrm{Arg}(A(\boldsymbol{Q}))$, is lost during the measurement[14]. This is known as the phase problem in scattering and diffraction measurements. Nevertheless, one can solve for $S(\boldsymbol{r})$ through an iterative phase retrieval process if the oversampling requirement is met[15–17]. In BCDI, this condition is satisfied by measuring the diffraction intensity with at least two pixels per interference fringe[4,15,18].

In the iterative phase retrieval, one updates both $A(\boldsymbol{Q})$ and $S(\boldsymbol{r})$ each cycle, where the Fourier transform connects the real space to the reciprocal space via eq. (1) and its inverse (Fig. 1). The measured 3D diffraction data $I(\boldsymbol{Q})$ imposes the reciprocal space constraint, and a 3D 'support' requires $S(\boldsymbol{r})$ to exist only inside the 'support' in the real space. The most commonly used algorithms are the error-reduction algorithm (ER)[19,20], the hybrid-input-output algorithm (HIO)[20], the difference map algorithm[21], and the relaxed-averaged-alternating-reflection algorithm (RAAR)[22]. Common phase retrieval practice in BCDI alternates between various algorithms to avoid stagnation in a local minimum and maintain efficient optimization. Because the shape of the crystal is unknown a priori, one updates the support via the Shrinkwrap algorithm during the iterative procedure[23]. Recently developed guided algorithms combine multiple results reconstructed separately and use them as the initial condition for the next set of iterations, which have shown consistent results for defect imaging[24–26].

The phase retrieval process yields the reconstructed complex density function $S(\boldsymbol{r})$ within the coordinate system defined by the slices of the Ewald sphere. To interpret the results and perform further analysis, it is common to convert the complex density function into the lab frame or a coordinate system in which the scattering vector direction is along the reciprocal lattice vector $\boldsymbol{h}$. Details and numerical implementation for coordinate transformation are described elsewhere[27,28]. The amplitude of the reconstructed $S(\boldsymbol{r})$, $s_{\boldsymbol{h}}(\boldsymbol{r})$, typically reports the shape of the crystal and resolves its facets[29]. It can also indicate defects, which result in zero intensity of $s_{\boldsymbol{h}}(\boldsymbol{r})$ since the periodicity of the scattering planes is disrupted. The phase, $\varphi(\boldsymbol{r}) = \mathrm{Arg}\,(S(\boldsymbol{Q}))$, encodes information of the displacement field, $\boldsymbol{u}(\boldsymbol{r})$, projected onto the reciprocal space vector, $\boldsymbol{h}$[4,12].

Having a non-zero displacement field in a crystal does not necessarily imply the presence of lattice distortions. A crystal with a perfect lattice can have a constant randomly assigned phase shift during the phase retrieval process. Instead, defects generally lead to a spatially varying displacement field[30]. Thus, taking the spatial derivative of the displacement field allows for a better identification of defects. We can calculate the normal strain along the reciprocal lattice vector, $\varepsilon_{\boldsymbol{h}}(\boldsymbol{r})$,

$$\varepsilon_{\boldsymbol{h}}(\boldsymbol{r}) = \frac{1}{|\boldsymbol{h}|}\left(\frac{\partial \boldsymbol{u}_{\boldsymbol{h}}}{\partial x_{\boldsymbol{h}}}\right)$$

where x points along the reciprocal space vector $\boldsymbol{h}$. The normal strain shows relative deviations in the lattice parameter. Additionally, one can calculate the derivative of the displacement perpendicular to $\boldsymbol{h}$, which adds to existing defect analysis to estimate shear stresses and identify dislocations[31]. The latter is only an estimate because multiple reciprocal lattice vectors are required to measure the shear stress. Defect types that are probed by BCDI include dislocations, twin boundaries, bulk strain induced by intercalation, and surface strain from adsorption (Fig. 1).

Recent advancements in BCDI techniques aim at probing materials under more diverse environments and extracting complete structural information. Newton *et al.* demonstrated a multi-reflection BCDI experiment, where they measured reciprocal maps around six reciprocal lattice points and imaged the full strain tensor[13]. Cha *et al.* implemented the variable-wavelength BCDI, where instead of rocking the sample, they scanned the energy of the incident x-ray beam[32]. The energy scanning can be beneficial because no sample motion is required, and the reconstructions show similar strain sensitivity as the conventional rocking-curve-based BCDI. Another approach to minimize sample instability is to adopt a continuous scanning mode, which compared to step-by-step scanning, can reduce the scan time by 30% and limit sample drift during the measurement, facilitating more accurate BCDI measurements for faster dynamics[33].

Along with the development of advanced experimental techniques, there is an ongoing effort to develop phase retrieval algorithms to accommodate more complex diffraction data. For example, Wang *et al.* developed an algorithm to simultaneously reconstruct multiple diffraction patterns of the same particle and successfully imaged the phase-coexistence during a simulated structural phase transformation[34]. This correlated phase retrieval algorithm was recently applied to experimental *operando* BCDI data to image a structural phase transformation of the high-voltage cathode $Li_xNi_{0.5}Mn_{1.5}O_4$[35]. Phase retrieval algorithms were also developed for multi-reflection

BCDI. By reconstructing multiple Bragg peaks concurrently, these algorithms have the potential to image data that are challenging to reconstruct with conventional approaches, such as the diffraction from highly strained crystals[36–39].

III. Applications

3.1 Ex-situ studies around a single reciprocal lattice point

In the most common type of BCDI, a reciprocal space map around a single reciprocal lattice point is investigated. Given its relatively low diffraction intensity from a small crystal with a size less than 1 μm, the oversampling requirement of BCDI is most likely fulfilled by high-density crystalline materials. Among them, gold, platinum, or palladium nanoparticles are often used. One of the first demonstrations of BCDI was performed on free-standing gold nanoparticles by Williams *et al*[9]. Recent studies on gold nanoparticles have investigated more complicated microstructures. For example, Ulvestad *et al.* elucidated a twin domain structure inside a gold nanocrystal. While aligned to the reciprocal lattice of one twin structure, the other twin structure appeared as a void in the reconstructed Bragg plane density[40]. In addition, the twinned domains interrupted the stacking order of the crystal, causing a phase offset that was directly observed in the displacement field. In another study, Choi *et al.* applied BCDI on chiral gold nanoparticles, where they successfully resolved more structurally complex 432 helicoid III and determined high Miller-index planes corresponding to the concave gap structures (Fig. 2b)[41]. In a recent work by Richard *et al.*, an anomalous {110}-type of glide plane was observed in platinum crystals in contrast to the expected {111} glide planes in FCC systems[42]. The glide plane was associated with preferential nucleation of defects at the surface of the crystals.

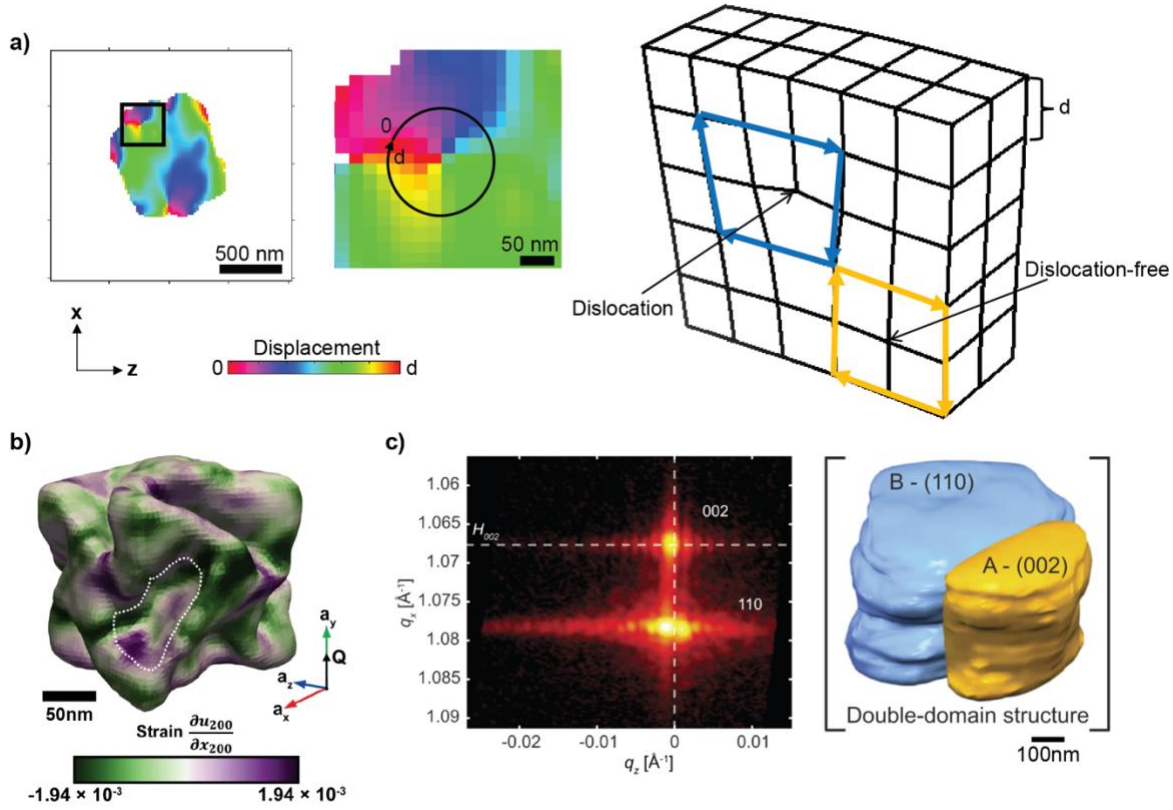

Figure 2. Ex-situ BCDI on nanocrystals of functional materials. **a)** (left) A 2D reconstructed displacement field of a single $Li_{7-3x}Al_xLa_3Zr_2O_{12}$ grain embedded in a pellet. (middle) The enlarged image of the black square in the left figure. At the singularity (center of the loop indicated by the black circle), the displacement field is discontinuous: it changes by one lattice spacing *d* when tracked along the loop. (right) The schematic of an edge dislocation and the Burgers circuit constructions. The displacement along the loop in a dislocation-free crystal (yellow) is continuous, while the loop around a dislocation (blue) result in an extra spacing along the Burgers vector. Reprinted with permission from Sun *et al.*, Nano Letters **21**, (2021). Copyright 2021 American Chemical Society. **b)** Reconstructed morphology and surface strain of the chiral gold nanoparticle, 432 helicoid III. Reprinted with permission from Choi *et al.*, Nat Commun **14**, (2023). Copyright 2023 Springer Nature. **c)** (left)The 2D projection of the reciprocal space intensity (log-scale) distribution of the (002) and (110) Bragg peaks of $CsPbBr_3$. (right) Reconstructed morphology of the double domain structure retrieved from the diffraction pattern. Reprinted with permission from Dzhigaev *et al.*, New J. Phys. **23**, 063035 (2021). Copyright 2021 Institute of Physics.

Characterization of structures and defects at the nanoscale for energy storage materials is critical as defects influence nanomaterials' mechanical, electrochemical, and kinetic properties differently from those of their bulk counterparts. BCDI is ideal for this type of characterization since the size of the nanoparticulate energy storage materials aligns exceptionally well with the capability of BCDI measurements. For example, most cathode materials for lithium and sodium-ion batteries consist of crystalline particles that are a few hundred nm large. In an ex-situ study for high-voltage cathode nanoparticles, $Li_xNi_{0.5}Mn_{1.5}O_4$, the reconstructed strain maps showed regions of compressive/tensile strain on the surface, which was connected to the local lithium concentration and interpreted as a local Jahn-Teller distortion of Mn cations[43]. In another study, Shabalin *et al.* mapped the 3D position of particles in a thick $Li_xNi_{0.5}Mn_{1.5}O_4$ cathode based on precise alignment with the instrument's axis of rotation, which had important applications in systems where the material's response to stimuli was not uniform[44]. Beyond cathode materials,

Sun *et al.* investigated a garnet-type solid-state electrolyte, $Li_{7-3x}Al_xLa_3Zr_2O_{12}$ (LLZO), at three levels of Al doping[45]. The reconstructed displacement field showed singularities in the cubic and mixed structural phases, indicating the presence of dislocations. These singularities were arranged along the dislocation line. Around any arbitrary loop centered at the dislocation line, the displacement field changed from 0 to b, where b is the burgers vector. This is equivalent to Burgers circuit construction of an edge dislocation (Fig. 2a). The analysis of dislocation-based singularities can be done directly on the displacement field determined via BCDI[12,46–48].

Another important class of materials investigated via BCDI is nanoparticles for electronic applications. The domain structure is particularly important as it influences polarization switching and electrical control in devices. Dzhigaev *et al.* measured the diffraction pattern on $CsPbBr_3$ nanocrystals, notable for their application in optoelectronic devices[49]. In the data, two peaks (the 002 and 110 peaks) of the same crystal coexisted in proximity, indicating twinned domains (Fig. 2c). By reconstructing the two peaks separately, they showed the double domain structure and a sharp domain boundary along the (112) plane (Fig. 2c). The presence of multiple peaks indicative of domain structure was also reported in InP nanocrystals[50]. The twin structure can also manifest itself in the reconstructed displacement field where domains are characterized by different lattice displacements[51–53]. In addition to the domain structure, mixed dislocations were observed in V_2O_3 nanocrystals by taking the azimuthal scan of displacement around the dislocation line, which showed components from both edge and screw dislocations[54]. BCDI has also shown promising results in more complex microstructures. For example, Shi *et al.* conducted a BCDI study on single core-shell Ni nanoparticles and observed edge dislocations in the shell region and at the boundary between the core and shell[55].

Aside from nanocrystals, many research groups have endeavored to employ BCDI for resolving strain and defects in nanowires. For instance, Schold *et al.* used BCDI to look at photoferroelectric SbSI nanowires and discovered planar defects that separated the wire into regions of positive and negative shear strain[56]. The coherency strain from the lattice mismatch between the core and shell materials can also be revealed by BCDI. Hill *et al.* employed BCDI strain mapping to determine the critical thickness of InGaAs quantum wells grown on GaAs nanowires, as well as to observe twinning and dislocations along the nanowire[57]. In a model piezotronic system consisting of a ZnO rod coated by a thin layer of gold as contacts, strain was found at the ZnO/Au interface and also inside the rod[58]. Similar behaviors of contact-induced strain were also observed in GaN nanowires[59]. Also in GaN nanowires, an inversion domain boundary, referring specifically to the interface between two opposite orientation domains of the hexagonal lattice, was identified in the displacement field from the BCDI measurement, which could affect the material's electrical and optical properties[60].

3.2 Ex-situ studies around multiple reciprocal lattice points

An extension of the ex-situ BCDI experiments that warrants further discussion is the multi-reflection BCDI experiment. A typical BCDI measurement investigates one diffraction peak from a nanocrystal, which only provides structural information along one specific scattering direction. By calculating the orientation matrix and carefully aligning the diffractometer, Newton *et al.* managed to measure six Bragg reflections from a free-standing ZnO nanocrystal and image the full strain tensor with BCDI[13]. More recently, Hofmann *et al.* used Laue diffraction to

determine the lattice orientation prior to BCDI and used multi-reflection BCDI to reveal a heterogeneous strain in ion-implanted gold and tungsten nanocrystals[61,62]. Another method to determine the orientations is to use electron backscatter diffraction (EBSD), which was applied on Fe-Ni and Co-Fe alloy microcrystals before multi-reflection BCDI measurements[63]. Using a FIB to specifically select samples with dislocations, Hofmann *et al.* measured six Bragg reflections from a micron-sized tungsten crystal and resolved all dislocations within the crystal, along with their 3D morphology and Burgers vector (Fig. 3)[64]. In another multi-reflection BCDI study on iron irradiated chromium nanocrystals, the reconstructed electron density showed voids that self-organized into void lattices and the calculated strain tensor indicated depth-dependent heterogeneity in the sample[65].

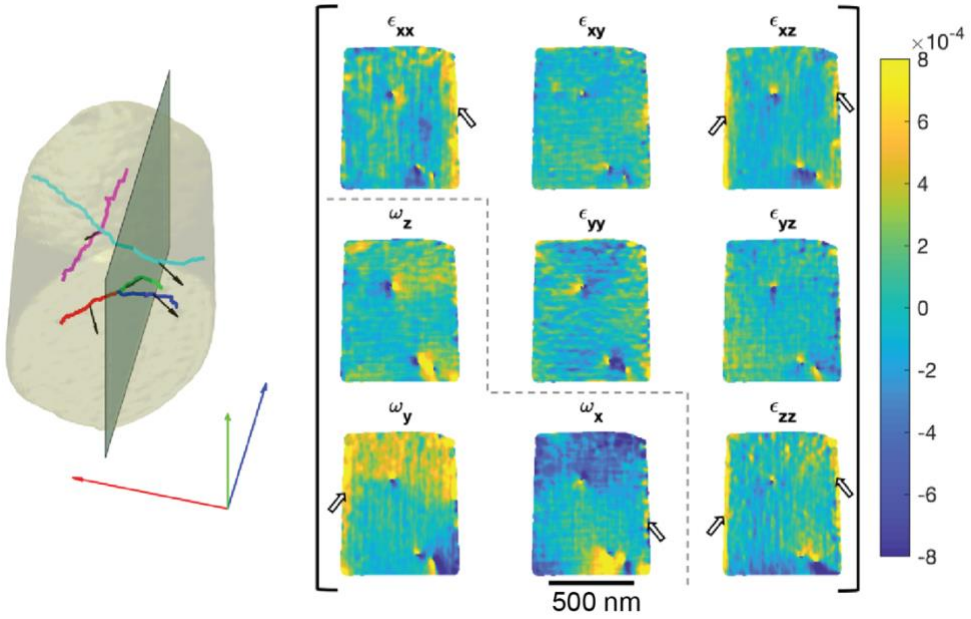

Figure 3. Multi-reflection Bragg Coherent Diffractive Imaging. (left) Rendering of a single tungsten nanocrystal showing dislocation lines (colored lines) and Burgers vectors (black arrows). Superimposed in green is the y-z plane on which strains are plotted. (right) The six components of the lattice strain tensor (upper triangle and diagonal), and the three components of the lattice rotation tensor (lower triangle) measured with multi-reflection BCDI. The strain fields of dislocations can be readily identified. Hollow arrows point to the surface strain associated with residual damage that occurred during the focused ion beam cutting of the particle. Reprinted with permission from Hofmann *et al.*, Phys. Rev. Mater. **4**, 013801 (2020).Copyright 2020 American Physical Society.

Many research efforts are underway to further advance the multi-reflection BCDI technique. In terms of phase retrieval for multi-reflection BCDI, Wilkin *et al.* employed a coupled genetic reconstruction algorithm and showed its efficacy on Au nanoparticles using both simulated and experimental datasets[38]. Moreover, multi-reflection BCDI has also shown potential in studying physical processes in situ and *operando*. Lauraux *et al.* demonstrated the feasibility of simultaneously measuring two independent Bragg peaks on a twinned Au crystal and scanning across incident X-ray energy, thereby circumventing the need to rock the sample differently for the two reflections[66]. The removal of the sample rocking step is expected to facilitate future multi-reflection BCDI experiments to resolve the strain tensor under external stimuli. Additionally, advancements in beamline instrumentation have facilitated the integration of Laue

diffraction into BCDI experiments, streamlining the workflow for multi-reflection BCDI studies[67].

3.3 In-situ studies

As BCDI continues to advance, more recent works have focused on in-situ studies of nanoparticles to uncover the strain and defect dynamics in response to external stimuli. These in-situ and *operando* measurements need to probe devices, which typically embed many nanocrystals. When the X-ray beam illuminates these nanoparticle ensembles, diffraction from many nanocrystals is observed. Due to the random orientation of the nanocrystals and the high angular sensitivity of Bragg diffraction, it is possible to isolate the coherent X-ray diffraction pattern from a single crystal. Nevertheless, in experimental setups, while ideally only the diffraction from a single crystal is recorded, signals from other crystals are often present in the measurements. Hence, the removal of these 'alien' intensities[68] is necessary before the phase retrieval. Here, we divide BCDI in-situ studies into two parts. The first part reviews studies that use bulk stimuli to induce structural changes across the crystal, while the second part focuses on studies investigating the surface structural evolution resulting from chemical reactions.

3.3.1 Bulk stimuli

Structural response to temperature is critical in materials processing such as annealing, sintering, and operation at high temperatures. Cha *et al.* investigated the microstructural evolution of zeolites, a crystalline aluminosilicate mineral, through heating under different calcination conditions[69]. The internal displacement mapping showed that the crystal adopted a transient triangular deformation from the core-shell arrangement of strain before full calcination. Yang *et al.* measured two independent reflections of FIB-milled gold microcrystals during annealing and demonstrated the role of annealing in decreasing strain heterogeneity and removal of defects[70]. Ulvestad *et al.* developed grain BCDI (gBCDI) to look at not only defect dynamics in individual grains but also changes at the grain boundary[71]. They revealed mobile coherent twin boundaries and dislocations that could locally enhance grain growth. In another study on single-grain growth in the transparent conduction oxide film, In_2O_3:Zr, Dzhigaev *et al.* reconstructed the same grain from sub-80 nm to 400 nm fully crystallized state under isothermal annealing and implemented the reconstructed strain field into models to study the kinetics of grain growth[72].

Temperature-induced structural phase transitions are important phenomena in materials science and are usually accompanied by nucleation of defects. In the tetragonal-to-cubic phase transformation of perovskite $BaTiO_3$, Diao *et al.* used BCDI to image the relative displacement of the twin domains and their domain boundary (Fig. 4a)[73]. The twinning and domain boundary disappeared as $BaTiO_3$ transitioned into the cubic phase upon heating, only to reemerge after cooling back to the tetragonal phase (Fig. 4a). Above the phase transition temperature, strain stripes of 30~50 nm wide were also observed in $BaTiO_3$[74]. The M_1 to M_2 structural phase transition in VO_2 nanocrystals during heating was also investigated with BCDI, and the 3D diffraction pattern revealed a progressive increase of distortion during heating, indicating the presence of strain gradients[75]. Incorporating a cryostat into BCDI beamlines allows further investigation of phase transitions in the low-temperature regime. During the transition to the low-temperature orthorhombic phase of the high-temperature superconductor $La_{2-x}Ba_xCuO_4$ (LBCO), Assefa *et al.* observed peak splitting in the diffraction pattern that indicated the formation of twin

domains and reconstructed the displacement field that showed a phase shift between the neighboring domains[76]. Upon repeating cooling and heating, a unique signature of the domain texture was present in the 3D speckle distribution in the diffraction of LBCO, providing evidence for domain pinning during the phase transition[77].

Laser and light stimuli are also used to induce lattice dynamics in nanocrystals that can be simultaneously probed by BCDI. Using an optical laser pump to induce lattice distortions in gold nanocrystals, Clark *et al.* measured the 3D diffraction pattern and successfully inverted these into changes of the displacement field on the picosecond timescale. They identified various breathing modes of the nanocrystal and an additional shear vibration mode[78]. A similar study was conducted on the model core/shell semiconductor-metal (ZnO/Ni) nanorod by Cherukara *et al.*, where they showed a rich interplay of radial, axial, and shear deformation modes at different timescales due to the strain from the Ni shell[79]. Light can also provide sufficient energy to mobilize defects such as dislocations. Orr *et al.* used BCDI to track the strain field in a halide perovskite microcrystal, $MAPbBr_3$ ($MA = CH_3NH_3^+$), and identified the extensive migration of edge dislocations with a <100> Burgers vector under illumination[80]. This process was associated with the degradation of halide perovskite materials and had critical implications for their optoelectronic properties.

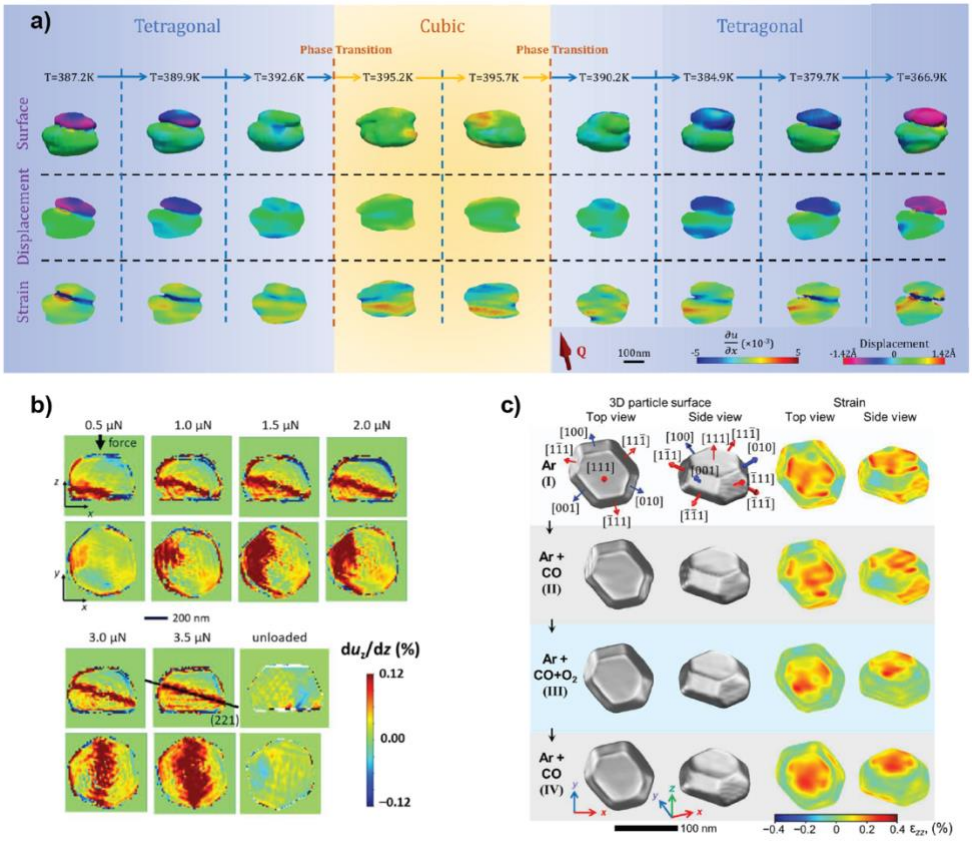

Figure 4. In-situ BCDI on nanocrystals during heating, mechanical loading, and surface oxidation. **a)** Images of a $BaTiO_3$ nanoparticle upon crossing through its tetragonal-cubic phase transition. The top row is a series of contour views of the reconstructed isosurface. The second row shows phase (displacement) cross-section maps taken in the

middle of the nanocrystal, while the bottom row shows strain (a derivative of displacement along reciprocal lattice vector) maps. Reprinted with permission from Diao *et al*., Phys. Rev. Materials **4**, 106001 (2020). Copyright 2020 American Physical Society. **b)** Reconstructed out-of-plane strain field in the Au crystal during nano-indentation. x, y, and z axis correspond to the [112], [110], and [111] crystallographic directions, respectively. Reprinted with permission from Lauraux *et al*., Materials **15**, 6195 (2022). Copyright 2022 Multidisciplinary Digital Publishing Institute. **c)** (left) Top and side views of the reconstructed shape of the nanoparticle and (right) strain fields, ε_{zz}, at the nanoparticle surface for gas conditions (I to IV). Reprinted with permission from Kim *et al*., Science Advances **7**, eabh0757 (2021). Copyright 2021 American Association for the Advancement of Science.

So far, there are only a few in-situ BCDI demonstrations for processes under mechanical and electrical stimuli. Lauraux *et al.* conducted an in situ nanoindentation multi-wavelength BCDI on gold sub-micrometric crystal using a scanning force microscope as the indenter[81]. The strain mapping showed the propagation of a defect band on the (211) lattice plane towards the crystal center upon loading, which disappeared once the mechanical force was released (Fig. 4b). Lazarev *et al.* demonstrated a BCDI measurement on GaN nanowires under an applied voltage bias, and the diffraction pattern revealed an increase of the bending angle due to the contacts at increasing voltage[82]. Kawaguchi *et al.* probed the strain evolution in Pt-Ni alloy nanoparticles during voltammetric cycling and showed the formation of tensile strain induced by the Pt shell[83]. These studies opened new avenues for in-situ BCDI measurements in exploring the dynamic structural behavior of functional materials.

3.3.2 Surface reactions

Probing structural dynamics under different chemical environments provides both a fundamental understanding of important processes such as crystal growth and corrosion and applicable design principles for electrochemical systems. Clark *et al.* employed BCDI to study the dislocation networks of calcite crystals during growth and dissolution, where the defect network distribution dictated the rapidly growing directions[25]. Yang *et al.* studied the dissolution of a Co-Fe alloy microcrystal exposed to hydrochloric acid (HCl)[84]. By tracking the reconstructed morphology as a function of time, they found more rapid corrosion at the corners and edges of the crystal. Applying BCDI to study hydrogen-induced phase transformation in palladium nanoparticles, Ulvestad *et al.* corroborated strain distribution with concentration gradient inside the cubic palladium particle and calculated the time-time displacement correlation matrix that revealed signs of aging and avalanching during the transformation[85]. On the other hand, Suzana *et al.* investigated the tetragonal palladium nanoparticles and observed a concave portion on one of the (111) facets close to the region identified as the seed cursor[86]. The effect of hydration was explored by Gorobtsov *et al.*, where they characterized a single yttrium-doped barium zirconate crystal embedded in a pellet during hydration at 200 °C. They imaged the nucleation and evolution of dislocation networks that culminated in the subsequent cracking[87].

Catalytic activity is closely related to defects such as surface strain. Thus, BCDI emerges as a useful tool to explore redox processes through defect imaging. Researchers have investigated the strain dynamics of gold nanoparticles during a standard CO oxidation reaction, and the resolved anisotropic surface strain showed a close connection to active site formation[88,89]. Platinum (Pt) nanoparticles, another common catalyst, were also studied during CO oxidation at elevated temperatures using BCDI. The reconstructed shape and strain maps in Pt nanoparticles presented the migration of a twin boundary during the reaction that left remnant compressive strain[90,91].

Similar dependence on facet orientations during the evolution of surface and bulk strain was also observed in a single PtRh-alloy nanoparticle (Fig. 4c)[92].

In addition to the CO oxidation reaction, the structural and defect dynamics under other oxidation-reduction conditions have also been explored with BCDI. Choi *et al.* studied platinum nanoparticles exposed to H_2O_2[93]. They found an orientation-dependent behavior in the catalytic adsorption process, where they saw alternating strain distribution at the 111 Bragg reflection but minimal changes at the 200 Bragg reflection. Kim *et al.* looked at platinum nanoparticles under methane oxidation and showed that mobile defects originated from the initially strained domains inside the particle[94]. Dupraz *et al.* evaluated the surface morphology and internal strain distribution of platinum nanoparticles under different gas compositions to investigate the relationship between facet-related strain and reaction chemistry at elevated temperatures[95]. A recent study successfully imaged the strain evolution of a platinum nanoparticle in an in-situ flow cell and revealed adsorbate-induced surface strain at the edges and corners of the particle, pushing a step further to achieve *operando* measurements[96]. Beyond platinum nanoparticles, magnetite (Fe_3O_4) was also studied with BCDI during oxidative dissolution at both ambient conditions and high temperatures[97]. The analysis revealed that ambient magnetite displayed heterogeneous strain and dislocations, while the thermally oxidized magnetite exhibited more uniform strain distribution. Zeolites during deoxygenation and hydrocarbon adsorption have also been investigated with in-situ BCDI[98,99].

3.4 *Operando* studies

Operando studies are a special case of in-situ studies, in which a measurement occurs in a fully functioning multicomponent device under conditions similar to real-world applications. So far, *operando* BCDI has only been performed in a working battery cell. The key to *operando* BCDI is to provide a window for X-ray penetration in the cell, where studies have used either modified coin cells[100] or Argonne's multi-purpose for in situ X-ray (AMPIX) cells[101]. *Operando* BCDI was demonstrated in the high-voltage cathode nanoparticles, $Li_xNi_{0.5}Mn_{1.5}O_4$. The analysis of single-particle diffraction patterns upon charge and discharge revealed different phase transformation mechanisms, in which a two-phase reaction manifested into peak splitting whereas a continuous shift of the diffraction peak suggested a solid-solution reaction[102]. Tracking the strain evolution in $Li_xNi_{0.5}Mn_{1.5}O_4$, Ulvestad *et al.* observed strain stripes and coherency strain at the nanoscale[46]. During discharge, the reconstructed displacement field indicated the presence of dislocation networks inside $Li_xNi_{0.5}Mn_{1.5}O_4$, where the corresponding strain maps showed domains of the lithium-rich phase[47]. The phase coexistence and microstructural dynamics during the two-phase reaction of $Li_xNi_{0.5}Mn_{1.5}O_4$ were also recently explored by Sun *et al.* using the correlated phase retrieval algorithm[35].

In layered oxide materials, defects are often related to unstable electrochemical performances, and thus understanding the defect dynamics under *operando* conditions provides critical guidelines for future materials design. Using *operando* BCDI to look at lithium-rich layered oxides (LRLO), $Li_{1.2}Ni_{0.133}Mn_{0.533}Co_{0.133}O_2$ nanoparticles, Singer *et al.* directly observed the nucleation of a mobile dislocation network (Fig. 5a), suggesting a link between defects and voltage fades in the material and demonstrating a method to reverse the voltage fade[48].

Combining *operando* BCDI with multiscale X-ray diffraction techniques on LRLO, Liu *et al.* discovered the heterogeneous nature of the LRLO cathode from the displacement maps and proposed a new mesostructure design for stable electrochemical performances[103]. In another layered oxide cathode, $LiNi_{0.8}Mn_{0.1}Co_{0.1}O_2$ (NMC811), BCDI showed non-uniform inter- and intra-crystalline strain at all measured states of charge and presented evidence of screw dislocations at the crystal core, close to where crystal splitting originated[104]. On coated NMC811, Liu *et al.* found improved crystal quality as the displacement field showed no appearance of singularities, which is a common indicator of dislocations[105].

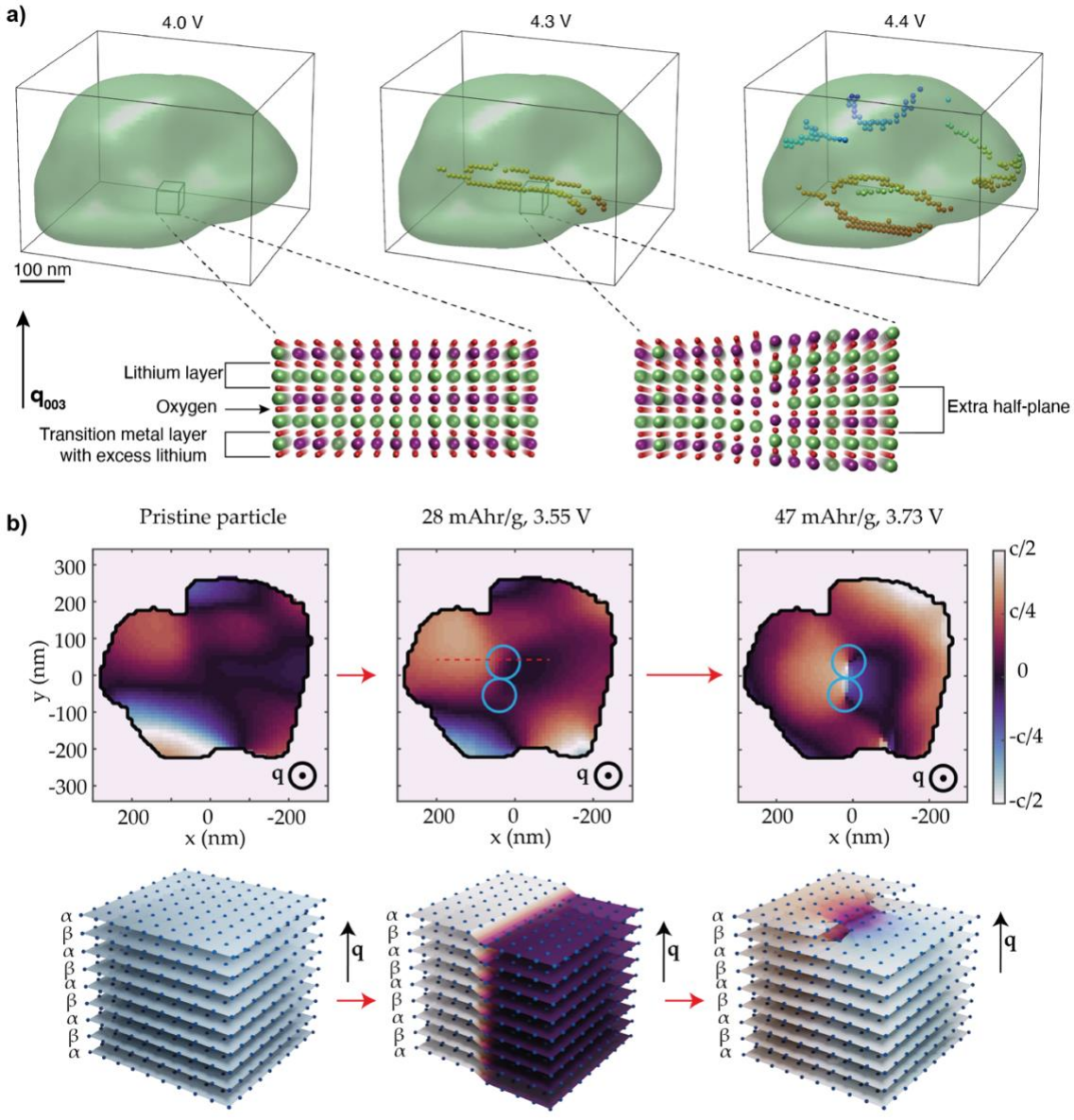

Figure 5. Operando BCDI on cathode nanoparticles in Li-ion and Na-ion batteries. **a)** Formation of a dislocation network during charge. At a charge state of 4.0 V versus Li^+, no dislocations are observed in the particle. The inset shows a schematic of a dislocation-free crystal. At 4.3 V, two edge dislocations have formed during lithium extraction. The inset shows a schematic of an edge dislocation. At 4.4 V, a dislocation network emerges (colors are used to represent different dislocations). Reprinted with permission from Singer *et al.*, Nature Energy **3**, (2018). Copyright 2018 Springer Nature. **b)** Dislocation pair nucleation on a domain border in P_2-$Na_{0.78}Ni_{0.23}Mn_{0.69}O_2$. (top)

Comparison of displacement cross-sections at different charge states. Appearance of two screw dislocations (top right) on the former domain boundary is visible (blue circles). (bottom) Schematic representation of a glissile dislocation loop nucleation on the domain boundary. Reprinted with permission from Gorobtsov *et al*., Advanced Energy Materials **13**, 2203654 (2023). Copyright 2023 Wiley-VCH.

Apart from lithium cathode nanoparticles, *operando* BCDI was also applied to other types of battery materials. Assefa *et al.* employed BCDI in lithium titanate (LTO) anode and elucidated the phase transformation of LTO during discharge, which manifested as distinct displacement modulation and the formation of 200 nm-sized phase domains[106]. Singer and Meng groups have further expanded BCDI for sodium-ion battery applications. In the study of two types of $Na_xNi_{1-y}Mn_yO_2$ intercalation hosts, Gorobtsov *et al.* captured the formation of a screw dislocation pair at the domain boundary (Fig. 5b) from the reconstructed displacement and strain field[107]. Subsequently, the dislocations migrated towards the edges of the particle. The transient nature of the defect indicated self-healing in sodium cathodes, which can only be observed by *operando* techniques. The work in Li-ion and Na-ion systems shows promising opportunities to further expand *operando* BCDI's applicability in energy storage systems based on different chemistries.

IV. Current limitations and future directions

Despite the extensive application of BCDI across various materials systems, several challenges remain. One key limitation lies in the size of the sample. It requires isolated nanocrystals large enough to give sufficient scattering signal, and the current coherent flux confines BCDI measurements to crystals larger than 50 nanometers. This poses a challenge as many technologically significant nanomaterials are considerably smaller. For instance, the catalytic nanoparticles in all current BCDI studies are significantly larger than the commercially used catalysts, which are typically a few nanometers large. Another example is the nanoprecipitates in metal alloys. Probing the defect structure of these nanoprecipitates requires inspection of superstructure reflections with intensities orders of magnitude lower than fundamental reflections[108]. Coupled with the small size of the precipitates, often less than 50 nm, this has precluded BCDI from resolving these nanoprecipitates in a disordered matrix. Nevertheless, the ongoing development of fourth-generation synchrotrons promises increasing flux, thereby paving the way for BCDI experiments to accommodate much smaller sample sizes[109].

BCDI also imposes a constraint on the maximum size of samples, typically around 1 μm. The limitation stems from several factors, including the transverse coherence of the X-ray beam, the ability to resolve interference fringes on the detector, and the need to maintain diffraction within the kinematic approximation. The new-generation synchrotron sources are nearly diffraction-limited and can provide highly coherent and bright beams, thereby alleviating the first limitation. Regarding the resolution of interference fringes, which decrease with increasing crystal size, larger sample-detector distances or smaller detector pixels are required. It has also been shown recently that BCDI can be applied to undersampled data[110,111]. In terms of kinematical diffraction, Shabalin *et al.* have demonstrated that dynamical effects became substantial when particle size approached 1 μm in palladium[112]. Gorobtsov *et al.* showed that the use of quasi-kinematical approximation can correct the dynamical effects for intermediately sized crystals[113]. In addition, high-index reflection can extend X-ray extinction length to mitigate the dynamical effects[114]. Pushing the ongoing development of brighter synchrotron sources will improve

BCDI's resolution to measure larger crystals. The enhanced resolution will also enable BCDI to offer insights comparable to X-ray surface scattering and crystal truncation rod analysis without the need to create and maintain high-quality surfaces, which can be quite demanding[115].

Another limitation, particularly evident in in-situ and *operando* BCDI, is the angular stability of the measured crystal. The rocking curves typically span angles of less than a degree[9], making even slight rotations susceptible to shifting the Bragg peak away from the Ewald sphere. During in-situ and *operando* measurements, uncontrolled nanoparticle rotations typically occur[35,46–48,102,107,116] due to factors such as heating, radiation pressure[117], or possibly electrolyte interaction. Although alignment scans can be conducted every few measurements to track the Bragg peak, the potential for small drifts during the scan remains unaccounted for. Despite that methods have been developed to recover 3D diffraction datasets from these uncontrolled and unpredictable rotations,[118], ongoing research is warranted to address these challenges effectively to enable BCDI applications in more dynamic environments.

For most BCDI measurements, establishing ground truth for validating reconstruction results from the phase retrieval process poses a significant challenge. Without a reference point, ensuring the reliability of results necessitates effective benchmarking practices across beamlines in the BCDI community. To validate their findings, researchers have relied on techniques such as averaging and comparing reconstructions of the crystal from phase retrieval procedures initiated from different starting conditions. Yet, this validation process has largely relied on subjective researcher judgment, introducing the potential for bias and inconsistency. While some endeavors have been made to introduce unbiased metrics for BCDI[119], propose the use of forward modeling as a cross-validation tool[114], and develop more automatic strain and defect analysis techniques[120,121], having a systematic validation of BCDI remains largely unexplored. Addressing this gap requires further investigation and discussion within the BCDI community to enhance the credibility and reliability of BCDI results.

With upgrades to diffraction-limited synchrotron sources and the use of BCDI at XFELs, the coherent X-ray flux will increase by two or three orders of magnitude, leading to a substantial rise in the size of BCDI datasets. The conventional iterative phase retrieval can become too time-consuming to handle such large amounts of data. Consequently, current research efforts in BCDI analysis focus on leveraging machine learning techniques. For instance, Cherukara *et al.* employed a pair of deep deconvolutional networks to predict the amplitude and phase separately based on 2D diffraction patterns[122]. In a similar vein, Wu *et al.* devised a neural network model capable of reconstructing complex images, later extending its application to three dimensions[123,124]. The need for a large volume of labeled data from simulations or prior experiments is particularly challenging for BCDI. To circumvent this problem, Yao *et al.* introduced AutoPhaseNN, an unsupervised physics-aware deep learning model trained solely on diffraction patterns, which demonstrated comparable performance to conventional phase retrieval algorithms on both simulated and experimental data[125]. Instead of recovering the crystal's displacement field, Lim *et al.* developed a defect classification model capable of directly predicting dislocations from the 3D coherent diffraction pattern[126]. While the iterative phase retrieval will likely remain valid as a final step of the BCDI reconstruction, machine learning models offer the advantage of significantly reduced processing time, enabling real-time feedback—an invaluable asset for conducting in situ and *operando* BCDI experiments at

upgraded synchrotrons such as the Advanced Photon Source Upgrade (APS-U)[127], the Extremely Brilliant Source at the European Synchrotron Research Facility (ESRF-EBS)[8] and other new generation x-ray sources.

Acknowledgments
The work was supported by the National Science Foundation under award number CAREER DMR-1944907. We thank Benjamin Gregory, Aileen Luo, and Yumeng Song for carefully reading the manuscript.

Data Availability
The data that support the findings of this study are available from the corresponding author upon reasonable request.

References

[1] N. Cherkashin, T. Denneulin, and M.J. Hÿtch, "Electron microscopy by specimen design: application to strain measurements," Sci Rep **7**(1), 12394 (2017).

[2] M. Verezhak, S. Van Petegem, A. Rodriguez-Fernandez, P. Godard, K. Wakonig, D. Karpov, V.L.R. Jacques, A. Menzel, L. Thilly, and A. Diaz, "X-ray ptychographic topography: A robust nondestructive tool for strain imaging," Phys. Rev. B **103**(14), 144107 (2021).

[3] A. Michelson, B. Minevich, H. Emamy, X. Huang, Y.S. Chu, H. Yan, and O. Gang, "Three-dimensional visualization of nanoparticle lattices and multimaterial frameworks," Science **376**(6589), 203–207 (2022).

[4] I. Robinson, and R. Harder, "Coherent X-ray diffraction imaging of strain at the nanoscale," Nature Mater **8**(4), 291–298 (2009).

[5] I. Robinson, J. Clark, and R. Harder, "Materials science in the time domain using Bragg coherent diffraction imaging," J. Opt. **18**(5), 054007 (2016).

[6] D. Karpov, and E. Fohtung, "Bragg coherent diffractive imaging of strain at the nanoscale," Journal of Applied Physics **125**(12), 121101 (2019).

[7] R.A. Vicente, I.T. Neckel, S.K.R.S. Sankaranarayanan, J. Solla-Gullon, and P.S. Fernández, "Bragg Coherent Diffraction Imaging for In Situ Studies in Electrocatalysis," ACS Nano **15**(4), 6129–6146 (2021).

[8] P. Raimondi, "ESRF-EBS: The Extremely Brilliant Source Project," Synchrotron Radiation News **29**(6), 8–15 (2016).

[9] G.J. Williams, M.A. Pfeifer, I.A. Vartanyants, and I.K. Robinson, "Three-Dimensional Imaging of Microstructure in Au Nanocrystals," Physical Review Letters **90**(17), 4 (2003).

[10] I.A. Vartanyants, and I.K. Robinson, "Partial coherence effects on the imaging of small crystals using coherent x-ray diffraction," Journal of Physics Condensed Matter, (2001).

[11] G. Friedel, "Sur les symétries cristallines que peut révéler la diffraction des rayons Röntgen," CR Acad. Sci. Paris **157**, 1533–1536 (1913).

[12] M.A. Pfeifer, G.J. Williams, I.A. Vartanyants, R. Harder, and I.K. Robinson, "Three-dimensional mapping of a deformation field inside a nanocrystal," Nature **442**(7098), 63–66 (2006).

[13] M.C. Newton, S.J. Leake, R. Harder, and I.K. Robinson, "Three-dimensional imaging of strain in a single ZnO nanorod," Nature Mater **9**(2), 120–124 (2010).

[14] J. Als-Nielsen, and D. Mcmorrow, *Elements of Modern X-Ray Physics Second Edition* (2011).

[15] D. Sayre, "Some implications of a theorem due to Shannon," Acta Cryst **5**(6), 843–843 (1952).

[16] J. Miao, D. Sayre, and H.N. Chapman, "Phase retrieval from the magnitude of the Fourier transforms of nonperiodic objects," J. Opt. Soc. Am. A, JOSAA **15**(6), 1662–1669 (1998).

[17] J. Miao, J. Kirz, and D. Sayre, "The oversampling phasing method," Acta Cryst D **56**(10), 1312–1315 (2000).

[18] R.H.T. Bates, "Fourier phase problems are uniquely solvable in more than one dimension. 1. Underlying theory.," Optik **61**, 247–262 (1982).

[19] R.W. Gerchberg, and W.O. Saxton, "A practical algorithm for the determination of phase from image and diffraction plane pictures.," Optik (Stuttgart), (1972).

[20] J.R. Fienup, "Phase retrieval algorithms: a comparison," Appl. Opt. **21**(15), 2758 (1982).

[21] V. Elser, "Phase retrieval by iterated projections," J. Opt. Soc. Am. A, JOSAA **20**(1), 40–55 (2003).

[22] D.R. Luke, "Relaxed averaged alternating reflections for diffraction imaging," Inverse Problems **21**(1), 37 (2004).

[23] S. Marchesini, H. He, H.N. Chapman, S.P. Hau-Riege, A. Noy, M.R. Howells, U. Weierstall, and J.C.H. Spence, "X-ray image reconstruction from a diffraction pattern alone," Phys. Rev. B **68**(14), 140101 (2003).

[24] C.C. Chen, J. Miao, C.W. Wang, and T.K. Lee, "Application of optimization technique to noncrystalline x-ray diffraction microscopy: Guided hybrid input-output method," Physical Review B - Condensed Matter and Materials Physics **76**(6), 064113 (2007).
[25] J.N. Clark, J. Ihli, A.S. Schenk, Y.Y. Kim, A.N. Kulak, J.M. Campbell, G. Nisbet, F.C. Meldrum, and I.K. Robinson, "Three-dimensional imaging of dislocation propagation during crystal growth and dissolution," Nature Materials **14**(8), 780–784 (2015).
[26] A. Ulvestad, Y. Nashed, G. Beutier, M. Verdier, S.O. Hruszkewycz, and M. Dupraz, "Identifying Defects with Guided Algorithms in Bragg Coherent Diffractive Imaging," Sci Rep **7**(1), 9920 (2017).
[27] S. Maddali, P. Li, A. Pateras, D. Timbie, N. Delegan, A.L. Crook, H. Lee, I. Calvo-Almazan, D. Sheyfer, W. Cha, F.J. Heremans, D.D. Awschalom, V. Chamard, M. Allain, and S.O. Hruszkewycz, "General approaches for shear-correcting coordinate transformations in Bragg coherent diffraction imaging. Part I," J Appl Cryst **53**(2), 393–403 (2020).
[28] P. Li, S. Maddali, A. Pateras, I. Calvo-Almazan, S.O. Hruszkewycz, W. Cha, V. Chamard, and M. Allain, "General approaches for shear-correcting coordinate transformations in Bragg coherent diffraction imaging. Part II," J Appl Cryst **53**(2), 404–418 (2020).
[29] I.K. Robinson, I.A. Vartanyants, G.J. Williams, M.A. Pfeifer, and J.A. Pitney, "Reconstruction of the shapes of gold nanocrystals using coherent x-ray diffraction," Physical Review Letters **87**(19), 1–4 (2001).
[30] W. Cha, S. Song, N.C. Jeong, R. Harder, K.B. Yoon, L.K. Robinson, and H. Kim, "Exploration of crystal strains using coherent x-ray diffraction," New Journal of Physics **12**, (2010).
[31] O. Gorobtsov, and A. Singer, "Shear displacement gradient in X-ray Bragg coherent diffractive imaging," J Synchrotron Rad **29**(3), 866–870 (2022).
[32] W. Cha, A. Ulvestad, M. Allain, V. Chamard, R. Harder, S.J. Leake, J. Maser, P.H. Fuoss, and S.O. Hruszkewycz, "Three Dimensional Variable-Wavelength X-Ray Bragg Coherent Diffraction Imaging," Phys. Rev. Lett. **117**(22), 225501 (2016).
[33] N. Li, M. Dupraz, L. Wu, S.J. Leake, A. Resta, J. Carnis, S. Labat, E. Almog, E. Rabkin, V. Favre-Nicolin, F.-E. Picca, F. Berenguer, R. van de Poll, J.P. Hofmann, A. Vlad, O. Thomas, Y. Garreau, A. Coati, and M.-I. Richard, "Continuous scanning for Bragg coherent X-ray imaging," Sci Rep **10**(1), 12760 (2020).
[34] Z. Wang, O. Gorobtsov, and A. Singer, "An algorithm for Bragg coherent x-ray diffractive imaging of highly strained nanocrystals," New Journal of Physics **22**(1), (2020).
[35] Y. Sun, S. Hy, N. Hua, J. Wingert, R. Harder, Y.S. Meng, O. Shpyrko, and A. Singer, "Operando real-space imaging of a structural phase transformation in a high-voltage electrode," (2023).
[36] Y. Gao, X. Huang, H. Yan, and G.J. Williams, "Bragg coherent diffraction imaging by simultaneous reconstruction of multiple diffraction peaks," Phys. Rev. B **103**(1), 014102 (2021).
[37] M.C. Newton, "Concurrent phase retrieval for imaging strain in nanocrystals," Phys. Rev. B **102**(1), 014104 (2020).
[38] M.J. Wilkin, S. Maddali, S.O. Hruszkewycz, A. Pateras, R.L. Sandberg, R. Harder, W. Cha, R.M. Suter, and A.D. Rollett, "Experimental demonstration of coupled multi-peak Bragg coherent diffraction imaging with genetic algorithms," Phys. Rev. B **103**(21), 214103 (2021).
[39] S. Maddali, T.D. Frazer, N. Delegan, K.J. Harmon, S.E. Sullivan, M. Allain, W. Cha, A. Dibos, I. Poudyal, S. Kandel, Y.S.G. Nashed, F.J. Heremans, H. You, Y. Cao, and S.O. Hruszkewycz, "Concurrent multi-peak Bragg coherent x-ray diffraction imaging of 3D nanocrystal lattice displacement via global optimization," Npj Comput Mater **9**(1), 1–12 (2023).
[40] A. Ulvestad, J.N. Clark, R. Harder, I.K. Robinson, and O.G. Shpyrko, "3D Imaging of Twin Domain Defects in Gold Nanoparticles," Nano Lett. **15**(6), 4066–4070 (2015).
[41] S. Choi, S.W. Im, J.-H. Huh, S. Kim, J. Kim, Y.-C. Lim, R.M. Kim, J.H. Han, H. Kim, M. Sprung, S.Y. Lee, W. Cha, R. Harder, S. Lee, K.T. Nam, and H. Kim, "Strain and crystallographic identification of the helically concaved gap surfaces of chiral nanoparticles," Nat Commun **14**(1), 3615 (2023).

[42] M.-I. Richard, S. Labat, M. Dupraz, J. Carnis, L. Gao, M. Texier, N. Li, L. Wu, J.P. Hofmann, M. Levi, S.J. Leake, S. Lazarev, M. Sprung, E.J.M. Hensen, E. Rabkin, and O. Thomas, "Anomalous Glide Plane in Platinum Nano- and Microcrystals," ACS Nano **17**(6), 6113–6120 (2023).
[43] A. Ulvestad, H.M. Cho, R. Harder, J.W. Kim, S.H. Dietze, E. Fohtung, Y.S. Meng, and O.G. Shpyrko, "Nanoscale strain mapping in battery nanostructures," Applied Physics Letters **104**(7), 073108 (2014).
[44] A.G. Shabalin, M. Zhang, W. Yao, R. Rysov, Z. Ren, D. Lapkin, Y.-Y. Kim, D. Assalauova, N. Mukharamova, M. Sprung, I.A. Vartanyants, Y.S. Meng, and O.G. Shpyrko, "Mapping the 3D position of battery cathode particles in Bragg coherent diffractive imaging," J Synchrotron Rad **30**(2), 445–448 (2023).
[45] Y. Sun, O. Gorobstov, L. Mu, D. Weinstock, R. Bouck, W. Cha, N. Bouklas, F. Lin, and A. Singer, "X-ray Nanoimaging of Crystal Defects in Single Grains of Solid-State Electrolyte Li7-3 xAlxLa3Zr2O12," Nano Letters **21**(11), 4570–4576 (2021).
[46] A. Ulvestad, A. Singer, H.M. Cho, J.N. Clark, R. Harder, J. Maser, Y.S. Meng, and O.G. Shpyrko, "Single particle nanomechanics in operando batteries via lensless strain mapping," Nano Letters **14**(9), 5123–5127 (2014).
[47] U. Ulvestad, A. Singer, J.N. Clark, H.M. Cho, J.W. Kim, R. Harder, J. Maser, Y.S. Meng, and O.G. Shpyrko, "Topological defect dynamics in operando battery nanoparticles," Science **348**(6241), 1344–1347 (2015).
[48] A. Singer, M. Zhang, S. Hy, D. Cela, C. Fang, T.A. Wynn, B. Qiu, Y. Xia, Z. Liu, A. Ulvestad, N. Hua, J. Wingert, H. Liu, M. Sprung, A.V. Zozulya, E. Maxey, R. Harder, Y.S. Meng, and O.G. Shpyrko, "Nucleation of dislocations and their dynamics in layered oxide cathode materials during battery charging," Nature Energy **3**(8), 641–647 (2018).
[49] D. Dzhigaev, Z. Zhang, L.A.B. Marçal, S. Sala, A. Björling, A. Mikkelsen, and J. Wallentin, "Three-dimensional coherent x-ray diffraction imaging of ferroelastic domains in single CsPbBr3 perovskite nanoparticles," New J. Phys. **23**(6), 063035 (2021).
[50] G. Niu, S.J. Leake, O. Skibitzki, T. Niermann, J. Carnis, F. Kießling, F. Hatami, E.H. Hussein, M.A. Schubert, P. Zaumseil, G. Capellini, W.T. Masselink, W. Ren, Z.-G. Ye, M. Lehmann, T. Schülli, T. Schroeder, and M.-I. Richard, "Advanced Coherent X-Ray Diffraction and Electron Microscopy of Individual InP Nanocrystals on Si Nanotips for III-V-on-Si Electronics and Optoelectronics," Phys. Rev. Appl. **11**(6), 064046 (2019).
[51] Z. Liu, E. Schold, D. Karpov, R. Harder, T. Lookman, and E. Fohtung, "Needle-Like Ferroelastic Domains in Individual Ferroelectric Nanoparticles," Advanced Electronic Materials **6**(5), 1901300 (2020).
[52] X. Shi, N.P. Nazirkar, Z. Barringer, S. Williams, R. Harder, and E. Fohtung, "Topological defects and ferroelastic twins in ferroelectric nanocrystals: What coherent X-rays can reveal about them," MRS Advances **7**(31), 899–904 (2022).
[53] A.F. Suzana, S. Liu, J. Diao, L. Wu, T.A. Assefa, M. Abeykoon, R. Harder, W. Cha, E.S. Bozin, and I.K. Robinson, "Structural Explanation of the Dielectric Enhancement of Barium Titanate Nanoparticles Grown under Hydrothermal Conditions," Advanced Functional Materials **33**(19), 2208012 (2023).
[54] Z. Barringer, J. Jiang, X. Shi, E. Schold, A. Pateras, S. Cipiccia, C. Rau, J. Shi, and E. Fohtung, "Imaging defects in vanadium(III) oxide nanocrystals using Bragg coherent diffractive imaging," CrystEngComm **23**(36), 6239–6244 (2021).
[55] X. Shi, R. Harder, Z. Liu, O. Shpyrko, E. Fullerton, B. Kiefer, and E. Fohtung, "Nanoscale Mapping of Heterogeneous Strain and Defects in Individual Magnetic Nanocrystals," Crystals **10**(8), 658 (2020).
[56] E. Schold, Z. Barringer, X. Shi, S. Williams, N.P. Nazirkar, Y. Wang, Y. Hu, J. Shi, and E. Fohtung, "Three-dimensional morphology and elastic strain revealed in individual photoferroelectric SbSI nanowire," MRS Bulletin **48**(5), 467–474 (2023).
[57] M.O. Hill, P. Schmiedeke, C. Huang, S. Maddali, X. Hu, S.O. Hruszkewycz, J.J. Finley, G. Koblmüller, and L.J. Lauhon, "3D Bragg Coherent Diffraction Imaging of Extended Nanowires: Defect Formation in Highly Strained InGaAs Quantum Wells," ACS Nano **16**(12), 20281–20293 (2022).

[58] P. Jordt, N. Wolff, S.B. Hrkac, S. Shree, D. Wang, R.J. Harder, C. Kübel, R. Adelung, O.G. Shpyrko, O.M. Magnussen, L. Kienle, and B.M. Murphy, "Visualizing Intrinsic 3D-Strain Distribution in Gold Coated ZnO Microstructures by Bragg Coherent X-Ray Diffraction Imaging and Transmission Electron Microscopy with Respect to Piezotronic Applications," Advanced Electronic Materials **7**(11), 2100546 (2021).
[59] S. Lazarev, Y.Y. Kim, L. Gelisio, Z. Bi, A. Nowzari, I.A. Zaluzhnyy, R. Khubbutdinov, D. Dzhigaev, A. Jeromin, T.F. Keller, M. Sprung, A. Mikkelsen, L. Samuelson, and I.A. Vartanyants, "Influence of Contacts and Applied Voltage on a Structure of a Single GaN Nanowire," Applied Sciences **11**(20), 9419 (2021).
[60] N. Li, S. Labat, S.J. Leake, M. Dupraz, J. Carnis, T.W. Cornelius, G. Beutier, M. Verdier, V. Favre-Nicolin, T.U. Schülli, O. Thomas, J. Eymery, and M.-I. Richard, "Mapping Inversion Domain Boundaries along Single GaN Wires with Bragg Coherent X-ray Imaging," ACS Nano **14**(8), 10305–10312 (2020).
[61] F. Hofmann, E. Tarleton, R.J. Harder, N.W. Phillips, P.-W. Ma, J.N. Clark, I.K. Robinson, B. Abbey, W. Liu, and C.E. Beck, "3D lattice distortions and defect structures in ion-implanted nano-crystals," Sci Rep **7**(1), 45993 (2017).
[62] N.W. Phillips, H. Yu, S. Das, D. Yang, K. Mizohata, W. Liu, R. Xu, R.J. Harder, and F. Hofmann, "Nanoscale lattice strains in self-ion implanted tungsten," Acta Materialia **195**, 219–228 (2020).
[63] D. Yang, M.T. Lapington, G. He, K. Song, M. Zhang, C. Barker, R.J. Harder, W. Cha, W. Liu, N.W. Phillips, and F. Hofmann, "Refinements for Bragg coherent X-ray diffraction imaging: electron backscatter diffraction alignment and strain field computation," J Appl Cryst **55**(5), 1184–1195 (2022).
[64] F. Hofmann, N.W. Phillips, S. Das, P. Karamched, G.M. Hughes, J.O. Douglas, W. Cha, and W. Liu, "Nanoscale imaging of the full strain tensor of specific dislocations extracted from a bulk sample," Phys. Rev. Mater. **4**(1), 013801 (2020).
[65] E. Jossou, T.A. Assefa, A.F. Suzana, L. Wu, C. Campbell, R. Harder, W. Cha, K. Kisslinger, C. Sun, J. Gan, L. Ecker, I.K. Robinson, and S.K. Gill, "Three-dimensional strain imaging of irradiated chromium using multi-reflection Bragg coherent diffraction," Npj Mater Degrad **6**(1), 1–11 (2022).
[66] F. Lauraux, S. Labat, S. Yehya, M.-I. Richard, S.J. Leake, T. Zhou, J.-S. Micha, O. Robach, O. Kovalenko, E. Rabkin, T.U. Schülli, O. Thomas, and T.W. Cornelius, "Simultaneous Multi-Bragg Peak Coherent X-ray Diffraction Imaging," Crystals **11**(3), 312 (2021).
[67] A. Pateras, R. Harder, W. Cha, J.G. Gigax, J.K. Baldwin, J. Tischler, R. Xu, W. Liu, M.J. Erdmann, R. Kalt, R.L. Sandberg, S. Fensin, and R. Pokharel, "Combining Laue diffraction with Bragg coherent diffraction imaging at 34-ID-C," J Synchrotron Rad **27**(5), 1430–1437 (2020).
[68] K. Pelzer, N. Schwarz, and R. Harder, "Removal of spurious data in Bragg coherent diffraction imaging: an algorithm for automated data preprocessing," J Appl Cryst **54**(2), 523–532 (2021).
[69] W. Cha, N.C. Jeong, S. Song, H. Park, T.C. Thanh Pham, R. Harder, B. Lim, G. Xiong, D. Ahn, I. McNulty, J. Kim, K.B. Yoon, I.K. Robinson, and H. Kim, "Core–shell strain structure of zeolite microcrystals," Nature Mater **12**(8), 729–734 (2013).
[70] D. Yang, N.W. Phillips, K. Song, R.J. Harder, W. Cha, and F. Hofmann, "Annealing of focused ion beam damage in gold microcrystals: an in situ Bragg coherent X-ray diffraction imaging study," J Synchrotron Rad **28**(2), 550–565 (2021).
[71] A. Yau, W. Cha, M.W. Kanan, G.B. Stephenson, and A. Ulvestad, "Bragg coherent diffractive imaging of single-grain defect dynamics in polycrystalline films," Science **356**(6339), 739–742 (2017).
[72] D. Dzhigaev, Y. Smirnov, P.-A. Repecaud, L.A.B. Marçal, G. Fevola, D. Sheyfer, Q. Jeangros, W. Cha, R. Harder, A. Mikkelsen, J. Wallentin, M. Morales-Masis, and M.E. Stuckelberger, "Three-dimensional in situ imaging of single-grain growth in polycrystalline In2O3:Zr films," Commun Mater **3**(1), 1–7 (2022).
[73] J. Diao, X. Shi, T.A. Assefa, L. Wu, A.F. Suzana, D.S. Nunes, D. Batey, S. Cipiccia, C. Rau, R.J. Harder, W. Cha, and I.K. Robinson, "Evolution of ferroelastic domain walls during phase transitions in barium titanate nanoparticles," Phys. Rev. Materials **4**(10), 106001 (2020).

[74] J. Diao, L. Wu, A.F. Suzana, E.S. Bozin, E.M. Zatterin, S.J. Leake, R.J. Harder, W. Cha, M. Abeykoon, J. Fan, H. Jiang, and I.K. Robinson, "Behavior of strain stripe networks in barium titanate nanocrystals on crossing its ferroelectric phase transition," Phys. Rev. Materials **8**(1), 016002 (2024).
[75] M. Newton, U. Wagner, and C. Rau, "Coherent X-ray diffraction of the M1 to M2 structural phase transition in a single vanadium dioxide nanocrystal," Appl. Phys. Express **15**(7), 077001 (2022).
[76] T.A. Assefa, Y. Cao, J. Diao, R.J. Harder, W. Cha, K. Kisslinger, G.D. Gu, J.M. Tranquada, M.P.M. Dean, and I.K. Robinson, "Scaling behavior of low-temperature orthorhombic domains in the prototypical high-temperature superconductor ${\mathrm{La}}_{1.875}{\mathrm{Ba}}_{0.125}{\mathrm{CuO}}_{4}$," Phys. Rev. B **101**(5), 054104 (2020).
[77] I. Robinson, T.A. Assefa, Y. Cao, G. Gu, R. Harder, E. Maxey, and M.P.M. Dean, "Domain Texture of the Orthorhombic Phase of La2−xBaxCuO4," J Supercond Nov Magn **33**(1), 99–106 (2020).
[78] J.N. Clark, L. Beitra, G. Xiong, A. Higginbotham, D.M. Fritz, H.T. Lemke, D. Zhu, M. Chollet, G.J. Williams, M. Messerschmidt, B. Abbey, R.J. Harder, A.M. Korsunsky, J.S. Wark, and I.K. Robinson, "Ultrafast Three-Dimensional Imaging of Lattice Dynamics in Individual Gold Nanocrystals," Science **341**(6141), 56–59 (2013).
[79] M.J. Cherukara, K. Sasikumar, A. DiChiara, S.J. Leake, W. Cha, E.M. Dufresne, T. Peterka, I. McNulty, D.A. Walko, H. Wen, S.K.R.S. Sankaranarayanan, and R.J. Harder, "Ultrafast Three-Dimensional Integrated Imaging of Strain in Core/Shell Semiconductor/Metal Nanostructures," Nano Lett. **17**(12), 7696–7701 (2017).
[80] K.W.P. Orr, J. Diao, M.N. Lintangpradipto, D.J. Batey, A.N. Iqbal, S. Kahmann, K. Frohna, M. Dubajic, S.J. Zelewski, A.E. Dearle, T.A. Selby, P. Li, T.A.S. Doherty, S. Hofmann, O.M. Bakr, I.K. Robinson, and S.D. Stranks, "Imaging Light-Induced Migration of Dislocations in Halide Perovskites with 3D Nanoscale Strain Mapping," Advanced Materials **35**(46), 2305549 (2023).
[81] F. Lauraux, S. Labat, M.-I. Richard, S.J. Leake, T. Zhou, O. Kovalenko, E. Rabkin, T.U. Schülli, O. Thomas, and T.W. Cornelius, "In Situ Nano-Indentation of a Gold Sub-Micrometric Particle Imaged by Multi-Wavelength Bragg Coherent X-ray Diffraction," Materials **15**(18), 6195 (2022).
[82] S. Lazarev, D. Dzhigaev, Z. Bi, A. Nowzari, Y.Y. Kim, M. Rose, I.A. Zaluzhnyy, O.Yu. Gorobtsov, A.V. Zozulya, F. Lenrick, A. Gustafsson, A. Mikkelsen, M. Sprung, L. Samuelson, and I.A. Vartanyants, "Structural Changes in a Single GaN Nanowire under Applied Voltage Bias," Nano Lett. **18**(9), 5446–5452 (2018).
[83] T. Kawaguchi, V. Komanicky, V. Latyshev, W. Cha, E.R. Maxey, R. Harder, T. Ichitsubo, and H. You, "Electrochemically Induced Strain Evolution in Pt–Ni Alloy Nanoparticles Observed by Bragg Coherent Diffraction Imaging," Nano Lett. **21**(14), 5945–5951 (2021).
[84] D. Yang, N. W. Phillips, K. Song, C. Barker, R. J. Harder, W. Cha, W. Liu, and F. Hofmann, "In situ Bragg coherent X-ray diffraction imaging of corrosion in a Co–Fe alloy microcrystal," CrystEngComm **24**(7), 1334–1343 (2022).
[85] A. Ulvestad, M.J. Welland, S.S.E. Collins, R. Harder, E. Maxey, J. Wingert, A. Singer, S. Hy, P. Mulvaney, P. Zapol, and O.G. Shpyrko, "Avalanching strain dynamics during the hydriding phase transformation in individual palladium nanoparticles," Nature Communications **6**, (2015).
[86] A.F. Suzana, L. Wu, T.A. Assefa, B.P. Williams, R. Harder, W. Cha, C.-H. Kuo, C.-K. Tsung, and I.K. Robinson, "Structure of a seeded palladium nanoparticle and its dynamics during the hydride phase transformation," Commun Chem **4**(1), 1–8 (2021).
[87] O. Gorobtsov, Y. Song, K. Fritz, D. Weinstock, Y. Sun, D. Sheyfer, W. Cha, J. Suntivich, and A. Singer, "In Situ Nanoscale Dynamics Imaging in a Proton-Conducting Solid Oxide for Protonic Ceramic Fuel Cells," Advanced Science **9**(25), 2202096 (2022).
[88] A.R. Passos, A. Rochet, L.M. Manente, A.F. Suzana, R. Harder, W. Cha, and F. Meneau, "Three-dimensional strain dynamics govern the hysteresis in heterogeneous catalysis," Nat Commun **11**(1), 4733 (2020).

[89] F. Meneau, A. Rochet, R. Harder, W. Cha, and A.R. Passos, "Operando 3D imaging of defects dynamics of twinned-nanocrystal during catalysis," J. Phys.: Condens. Matter **33**(27), 274004 (2021).
[90] M. Abuin, Y.Y. Kim, H. Runge, S. Kulkarni, S. Maier, D. Dzhigaev, S. Lazarev, L. Gelisio, C. Seitz, M.-I. Richard, T. Zhou, V. Vonk, T.F. Keller, I.A. Vartanyants, and A. Stierle, "Coherent X-ray Imaging of CO-Adsorption-Induced Structural Changes in Pt Nanoparticles: Implications for Catalysis," ACS Appl. Nano Mater. **2**(8), 4818–4824 (2019).
[91] J. Carnis, A.R. Kshirsagar, L. Wu, M. Dupraz, S. Labat, M. Texier, L. Favre, L. Gao, F.E. Oropeza, N. Gazit, E. Almog, A. Campos, J.-S. Micha, E.J.M. Hensen, S.J. Leake, T.U. Schülli, E. Rabkin, O. Thomas, R. Poloni, J.P. Hofmann, and M.-I. Richard, "Twin boundary migration in an individual platinum nanocrystal during catalytic CO oxidation," Nat Commun **12**(1), 5385 (2021).
[92] Y.Y. Kim, T.F. Keller, T.J. Goncalves, M. Abuin, H. Runge, L. Gelisio, J. Carnis, V. Vonk, P.N. Plessow, I.A. Vartaniants, and A. Stierle, "Single alloy nanoparticle x-ray imaging during a catalytic reaction," Science Advances **7**(40), eabh0757 (2021).
[93] S. Choi, M. Chung, D. Kim, S. Kim, K. Yun, W. Cha, R. Harder, T. Kawaguchi, Y. Liu, A. Ulvestad, H. You, M.K. Song, and H. Kim, "In Situ Strain Evolution on Pt Nanoparticles during Hydrogen Peroxide Decomposition," Nano Lett. **20**(12), 8541–8548 (2020).
[94] D. Kim, M. Chung, S. Kim, K. Yun, W. Cha, R. Harder, and H. Kim, "Defect Dynamics at a Single Pt Nanoparticle during Catalytic Oxidation," Nano Lett. **19**(8), 5044–5052 (2019).
[95] M. Dupraz, N. Li, J. Carnis, L. Wu, S. Labat, C. Chatelier, R. van de Poll, J.P. Hofmann, E. Almog, S.J. Leake, Y. Watier, S. Lazarev, F. Westermeier, M. Sprung, E.J.M. Hensen, O. Thomas, E. Rabkin, and M.-I. Richard, "Imaging the facet surface strain state of supported multi-faceted Pt nanoparticles during reaction," Nat Commun **13**(1), 3003 (2022).
[96] M.-I. Richard, I. Martens, M. Dupraz, J. Drnec, V. Honkimäki, C. Chatelier, C. Atlan, M. Mirolo, M. Levi, E. Rabkin, J. Eymery, A. Naidu, T.U. Schülli, and S.J. Leake, "Taking Bragg Coherent Diffraction Imaging to Higher Energies at Fourth Generation Synchrotrons: Nanoscale Characterization," ACS Appl. Nano Mater. **6**(12), 10246–10255 (2023).
[97] K. Yuan, S.S. Lee, W. Cha, A. Ulvestad, H. Kim, B. Abdilla, N.C. Sturchio, and P. Fenter, "Oxidation induced strain and defects in magnetite crystals," Nat Commun **10**(1), 703 (2019).
[98] J. Kang, J. Carnis, D. Kim, M. Chung, J. Kim, K. Yun, G. An, W. Cha, R. Harder, S. Song, M. Sikorski, A. Robert, N.H. Thanh, H. Lee, Y.N. Choi, X. Huang, Y.S. Chu, J.N. Clark, M.K. Song, K.B. Yoon, I.K. Robinson, and H. Kim, "Time-resolved in situ visualization of the structural response of zeolites during catalysis," Nat Commun **11**(1), 5901 (2020).
[99] J. Kang, Y.J. Kim, D. Kim, K. Yun, M. Chung, T.H. Nguyen, S.Y. Lee, K.B. Yoon, and H. Kim, "Strain Development of Selective Adsorption of Hydrocarbons in a Cu-ZSM-5 Crystal," ACS Appl. Mater. Interfaces **13**(43), 50892–50899 (2021).
[100] L. Li, Y. Xie, E. Maxey, and R. Harder, "Methods for operando coherent X-ray diffraction of battery materials at the Advanced Photon Source," J Synchrotron Rad **26**(1), 220–229 (2019).
[101] O.J. Borkiewicz, B. Shyam, K.M. Wiaderek, C. Kurtz, P.J. Chupas, and K.W. Chapman, "The AMPIX electrochemical cell: a versatile apparatus for in situ X-ray scattering and spectroscopic measurements," J Appl Cryst **45**(6), 1261–1269 (2012).
[102] A. Singer, A. Ulvestad, H.M. Cho, J.W. Kim, J. Maser, R. Harder, Y.S. Meng, and O.G. Shpyrko, "Nonequilibrium structural dynamics of nanoparticles in LiNi1/2Mn3/2O4 cathode under operando conditions," Nano Letters **14**(9), 5295–5300 (2014).
[103] T. Liu, J. Liu, L. Li, L. Yu, J. Diao, T. Zhou, S. Li, A. Dai, W. Zhao, S. Xu, Y. Ren, L. Wang, T. Wu, R. Qi, Y. Xiao, J. Zheng, W. Cha, R. Harder, I. Robinson, J. Wen, J. Lu, F. Pan, and K. Amine, "Origin of structural degradation in Li-rich layered oxide cathode," Nature **606**(7913), 305–312 (2022).
[104] A.K.C. Estandarte, J. Diao, A.V. Llewellyn, A. Jnawali, T.M.M. Heenan, S.R. Daemi, J.J. Bailey, S. Cipiccia, D. Batey, X. Shi, C. Rau, D.J.L. Brett, R. Jervis, I.K. Robinson, and P.R. Shearing, "Operando Bragg

Coherent Diffraction Imaging of LiNi0.8Mn0.1Co0.1O2 Primary Particles within Commercially Printed NMC811 Electrode Sheets," ACS Nano, 10 (2021).
[105] X. Liu, X. Zhou, Q. Liu, J. Diao, C. Zhao, L. Li, Y. Liu, W. Xu, A. Daali, R. Harder, I.K. Robinson, M. Dahbi, J. Alami, G. Chen, G.-L. Xu, and K. Amine, "Multiscale Understanding of Surface Structural Effects on High-Temperature Operational Resiliency of Layered Oxide Cathodes," Advanced Materials **34**(4), 2107326 (2022).
[106] T.A. Assefa, A.F. Suzana, L. Wu, R.J. Koch, L. Li, W. Cha, R.J. Harder, E.S. Bozin, F. Wang, and I.K. Robinson, "Imaging the Phase Transformation in Single Particles of the Lithium Titanate Anode for Lithium-Ion Batteries," ACS Appl. Energy Mater. **4**(1), 111–118 (2021).
[107] O.Yu. Gorobtsov, H. Hirsh, M. Zhang, D. Sheyfer, L.H.B. Nguyen, S.D. Matson, D. Weinstock, R. Bouck, Z. Wang, W. Cha, J. Maser, R. Harder, Y.S. Meng, and A. Singer, "Operando Interaction and Transformation of Metastable Defects in Layered Oxides for Na-Ion Batteries," Advanced Energy Materials **13**(21), 2203654 (2023).
[108] M. Dupraz, S.J. Leake, and M.-I. Richard, "Bragg coherent imaging of nanoprecipitates: role of superstructure reflections," J Appl Cryst **53**(5), 1353–1369 (2020).
[109] M.-I. Richard, S. Labat, M. Dupraz, N. Li, E. Bellec, P. Boesecke, H. Djazouli, J. Eymery, O. Thomas, T.U. Schülli, M.K. Santala, and S.J. Leake, "Bragg coherent diffraction imaging of single 20 nm Pt particles at the ID01-EBS beamline of ESRF," J Appl Cryst **55**(3), 621–625 (2022).
[110] S. Maddali, M. Allain, W. Cha, R. Harder, J.-S. Park, P. Kenesei, J. Almer, Y. Nashed, and S.O. Hruszkewycz, "Phase retrieval for Bragg coherent diffraction imaging at high x-ray energies," Phys. Rev. A **99**(5), 053838 (2019).
[111] S. Maddali, J.-S. Park, H. Sharma, S. Shastri, P. Kenesei, J. Almer, R. Harder, M.J. Highland, Y. Nashed, and S.O. Hruszkewycz, "High-Energy Coherent X-Ray Diffraction Microscopy of Polycrystal Grains: Steps Toward a Multiscale Approach," Phys. Rev. Appl. **14**(2), 024085 (2020).
[112] A.G. Shabalin, O.M. Yefanov, V.L. Nosik, V.A. Bushuev, and I.A. Vartanyants, "Dynamical effects in Bragg coherent x-ray diffraction imaging of finite crystals," Phys. Rev. B **96**(6), 064111 (2017).
[113] O.Yu. Gorobtsov, and I.A. Vartanyants, "Phase of transmitted wave in dynamical theory and quasi-kinematical approximation," Phys. Rev. B **93**(18), 184107 (2016).
[114] Y. Gao, X. Huang, R. Harder, W. Cha, G.J. Williams, and H. Yan, "Modeling and experimental validation of dynamical effects in Bragg coherent x-ray diffractive imaging of finite crystals," Phys. Rev. B **106**(18), 184111 (2022).
[115] T. Fuchs, J. Drnec, F. Calle-Vallejo, N. Stubb, D.J.S. Sandbeck, M. Ruge, S. Cherevko, D.A. Harrington, and O.M. Magnussen, "Structure dependency of the atomic-scale mechanisms of platinum electro-oxidation and dissolution," Nat Catal **3**(9), 754–761 (2020).
[116] J.J. Huang, D. Weinstock, H. Hirsh, R. Bouck, M. Zhang, O.Yu. Gorobtsov, M. Okamura, R. Harder, W. Cha, J.P.C. Ruff, Y.S. Meng, and A. Singer, "Disorder Dynamics in Battery Nanoparticles During Phase Transitions Revealed by Operando Single-Particle Diffraction," Advanced Energy Materials **12**(12), 2103521 (2022).
[117] J.W. Kim, A. Ulvestad, S. Manna, R. Harder, E. Fohtung, A. Singer, L. Boucheron, E.E. Fullerton, and O.G. Shpyrko, "Observation of x-ray radiation pressure effects on nanocrystals," Journal of Applied Physics **120**(16), 163102 (2016).
[118] A. Björling, L.A.B. Marçal, J. Solla-Gullón, J. Wallentin, D. Carbone, and F.R.N.C. Maia, "Three-Dimensional Coherent Bragg Imaging of Rotating Nanoparticles," Phys. Rev. Lett. **125**(24), 246101 (2020).
[119] V. Favre-Nicolin, S. Leake, and Y. Chushkin, "Free log-likelihood as an unbiased metric for coherent diffraction imaging," Sci Rep **10**(1), 2664 (2020).

[120] A. Ulvestad, M. Menickelly, and S.M. Wild, “Accurate, rapid identification of dislocation lines in coherent diffractive imaging via a min-max optimization formulation,” AIP Advances **8**(1), 015114 (2018).
[121] J. Carnis, L. Gao, S. Labat, Y.Y. Kim, J.P. Hofmann, S.J. Leake, T.U. Schülli, E.J.M. Hensen, O. Thomas, and M.-I. Richard, “Towards a quantitative determination of strain in Bragg Coherent X-ray Diffraction Imaging: artefacts and sign convention in reconstructions,” Sci Rep **9**(1), 17357 (2019).
[122] M.J. Cherukara, Y.S.G. Nashed, and R.J. Harder, “Real-time coherent diffraction inversion using deep generative networks,” Sci Rep **8**(1), 16520 (2018).
[123] L. Wu, P. Juhas, S. Yoo, and I. Robinson, “Complex imaging of phase domains by deep neural networks,” IUCrJ **8**(1), 12–21 (2021).
[124] L. Wu, S. Yoo, A.F. Suzana, T.A. Assefa, J. Diao, R.J. Harder, W. Cha, and I.K. Robinson, “Three-dimensional coherent X-ray diffraction imaging via deep convolutional neural networks,” Npj Comput Mater **7**(1), 1–8 (2021).
[125] Y. Yao, H. Chan, S. Sankaranarayanan, P. Balaprakash, R.J. Harder, and M.J. Cherukara, “AutoPhaseNN: unsupervised physics-aware deep learning of 3D nanoscale Bragg coherent diffraction imaging,” Npj Comput Mater **8**(1), 1–8 (2022).
[126] B. Lim, E. Bellec, M. Dupraz, S. Leake, A. Resta, A. Coati, M. Sprung, E. Almog, E. Rabkin, T. Schulli, and M.-I. Richard, “A convolutional neural network for defect classification in Bragg coherent X-ray diffraction,” Npj Comput Mater **7**(1), 115 (2021).
[127] M. Borland, and A. Blednykh, *The Upgrade of the Advanced Photon Source* (Brookhaven National Lab.(BNL), Upton, NY (United States), 2018).